

Design, Synthesis, and Characterization of Polymer Precursors to Li_xPON and Li_xSiPON Glasses: Materials That Enable All-Solid-State Batteries (ASBs)

Xinyu Zhang, Eleni Temeche, and Richard M. Laine*

Cite This: *Macromolecules* 2020, 53, 2702–2712

Read Online

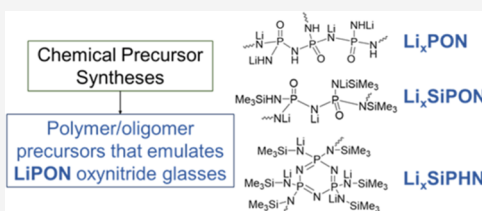
ACCESS |

Metrics & More

Article Recommendations

Supporting Information

ABSTRACT: LiPON -like glasses that form lithium dendrite impenetrable interfaces between lithium battery components are enabling materials that may replace liquid electrolytes permitting production of all-solid-state batteries (ASBs). Unfortunately, to date, such materials are introduced only via gas-phase deposition. Here, we demonstrate the design and synthesis of easily scaled, low-temperature, low-cost, solution-processable inorganic polymers containing $\text{LiPON}/\text{LiSiPON}$ elements. OPCl_3 and hexachlorophosphazene $[\text{Cl}_2\text{P}=\text{N}]_3$ provide starting points for elaboration using MNH_2 ($\text{M} = \text{Li}/\text{Na}$) or $(\text{Me}_3\text{Si})\text{NH}$ followed by reaction with controlled amounts of LiNH_2 to produce oligomers/polymers with molecular weights (MWs) $\approx 1\text{--}2$ kDa characterized by multinuclear NMR, gel permeation chromatography (GPC), thermogravimetric analysis (TGA), Fourier-transform infrared (FTIR), X-ray powder diffraction (XRD), X-ray photoelectron spectroscopy (XPS), and matrix-assisted laser desorption/ionization (MALDI)-time-of-flight (ToF) offering stabilities to $150\text{--}200^\circ\text{C}$ and ceramic yields (800°C) of $50\text{--}60\%$. ^7Li NMR suggests that precursor-bound Li^+ dissociates easily, beneficial for electrochemical applications. XPS shows higher N/P ratios ($1\text{--}3$) than via gas-phase methods (<1) correlating N/P ratios, ^7Li shifts, and Li^+ conductivities. Li_2SiPHN offers the highest ambient conductivity of $3 \times 10^{-1} \text{ mS cm}^{-1}$ at $400^\circ\text{C}/2 \text{ h/N}_2$.



INTRODUCTION

Microelectronic devices play an increasingly important role in our lives. The main component of these devices is the power source/energy-storage unit, the battery. Currently, rechargeable lithium-ion batteries are widely employed for their high energy densities and long cycle lives. Classical Li^+ batteries use liquid electrolytes that consist of inorganic salts dissolved in organic solvents, which often restrict their size, design, and have inherent safety risks that together restrain operating temperature windows.^{1,2} In contrast, solid-state electrolytes offer considerable design potential especially for miniaturization and/or scaling, improved safety, and a wider operating temperature window.^{2–5}

However, most solid electrolytes suffer from low ionic conductivities, a limited stability window, or from irreversible reduction [e.g., $\text{LASi}(\text{Ge})\text{TP}$ materials]^{6–11} on cycling or lithium dendrite growth along grain boundaries (e.g., LLZO materials)^{11–16} leading to short circuiting. Fortunately, amorphous lithium phosphorus oxynitride (Li_xPON) has been found to offer protection against both processes.^{9,16–19}

LiPON is one of the most commonly employed solid-state electrolytes owing to its broad electrochemical stability window ($0\text{--}5 \text{ V vs Li}^+/\text{Li}$),^{20,21} high critical current density ($>10 \text{ mA cm}^{-2}$),^{22–25} and negligible electronic conductivity ($10^{-7} \mu\text{S cm}^{-1}$).^{1,26,27} However, due to its limited ionic conductivity ($10^{-6} \text{ S cm}^{-1}$),^{1,20,21,26,28,29} its application is restricted to thin-

film batteries with limited energy densities and capacities.^{2,25,30,31}

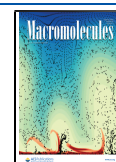
Recently, silicon-containing LiPON (or LiSiPON) has attracted attention due to its increased ionic conductivity induced by silicon doping. Lee et al.^{32,33} reported that LiSiPON films can reach $10^{-5} \text{ S cm}^{-1}$ at room temperature (RT) and increasing Si/P ratios reduce the activation energy for ionic transport. Su et al.³⁴ reported depositing LiSiPON thin films ($\sim 1 \mu\text{m}$) by radio frequency magnetron sputtering (RFMS) with ionic conductivities at ambient $\approx 10^{-5} \text{ S cm}^{-1}$ and an activation energy of 0.41 eV at $\text{Si}/\text{P} = 1$.

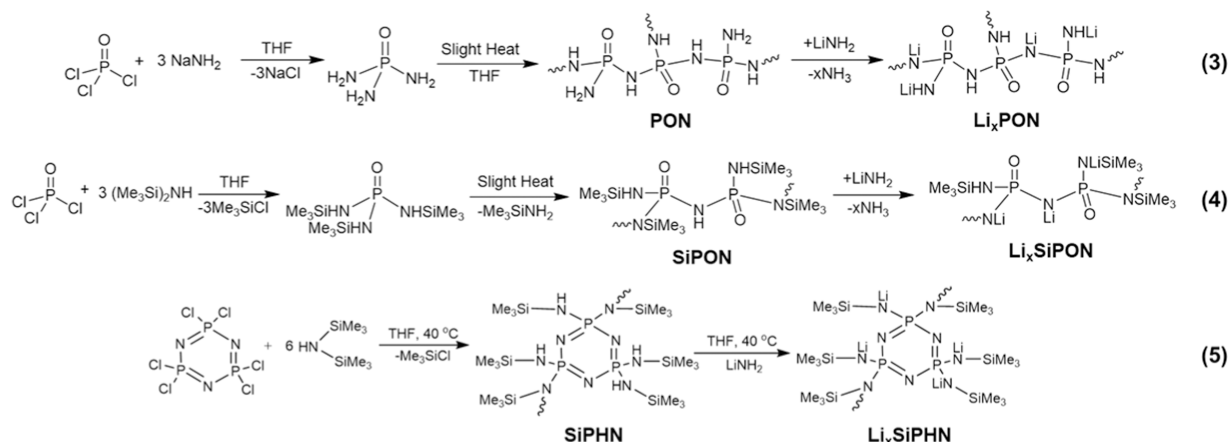
LiPON -like thin films are typically processed by gas-phase methods, such as RFMS,^{20,32–35} pulse laser deposition,³⁶ ion beam-assisted deposition,³⁷ plasma-assisted direct vapor deposition,³⁸ plasma-enhanced metalloorganic chemical vapor deposition,³⁹ atomic layer deposition,⁴⁰ etc. The main limitations of gas-phase deposition are low deposition rates (typically $<100 \text{ nm min}^{-1}$),^{35–38} the need for specialized apparatus, fabrication of large, homogeneous composition targets, and likely costly economics at commodity scales.

Received: February 1, 2020

Revised: March 2, 2020

Published: March 20, 2020



Scheme 1. Syntheses of Li_xPON , Li_xSiPON , and Li_xSiPHN Precursors ($x = \text{Li/P}$)

Thus, there are considerable economic and performance mandates driving the search for easier processing routes to the same materials especially for the practical processing of all-solid-state batteries (ASBs). The use of chemical precursor routes to the same materials seems to offer considerable potential to solve these issues.

The concept of designing ceramic materials “atom by atom” using molecular precursors had its origins in work published by Chantrell and Popper et al.⁴¹ and Aylett et al.⁴² in the mid 1960s but became main stream with a review by Wynne and Rice from the Office of Naval Research⁴³ and coincidental efforts by Ulrich et al. from the Air Force Office of Scientific Research through the “better ceramics through chemistry” symposia in the 1980s.^{44,45}

This field has progressed considerably since that time and there is now sufficient literature to allow development of design principles for generating precursors with multiple desirable properties including control of final elemental compositions, high ceramic yields (CYs) from initial components while engendering processability and minimizing unwanted off gassing of supporting moieties used to enhance processability.^{46–49} Based on these design principles, we have explored the development of LiPON and LiSiPON -like and Li_xSiPHN precursors and demonstrated their efficacy as ion-conducting polymers in Li-S half-cells.⁵⁰ These materials seem to offer properties superior to gas-phase-deposited LiPON materials.

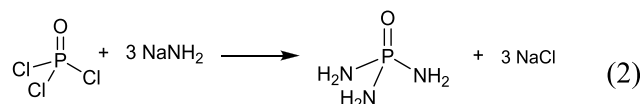
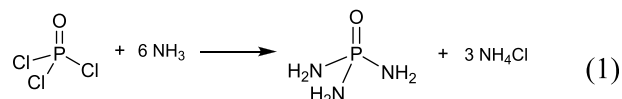
Our designed approach uses easily available starting materials, either OPCl_3 or $[\text{Cl}_2\text{P}=\text{N}]_3$. The logic behind the synthetic designs and approaches is detailed in the following sections. The resulting precursors are typically oligomers or low-molecular-weight (MW) polymers derived from lithiation of $\text{OP}(\text{NH}_2)_{3-x}(\text{NH})_x$ [from $\text{OP}(\text{NH})_3$], $\text{OP}(\text{NH}_2)_{3-x}(\text{NHSiMe}_3)_x$ and $[\text{P}=\text{N}]_3(\text{NHSiMe}_3)_{6-x}(\text{NH})_x$. Selected amounts of LiNH_2 provide varying degrees of lithiation and Li^+ -conducting properties commensurate with Li^+ content. When employed as Li^+ electrolytes impregnated in/on Celgard, Li^+ conductivities up to $\sim 1 \times 10^{-5} \text{ S cm}^{-1}$ at room temperature are obtained.⁵⁰

The current report presents in-depth characterization of the above-mentioned precursors providing detailed analyses of various structural components and Li^+ environments. A diverse set of analytical methods were used including gel permeation chromatography (GPC), thermogravimetric analysis (TGA), matrix-assisted laser desorption/ionization (MALDI), multi-nuclear magnetic resonance spectroscopy (NMR), and X-ray photoelectron spectroscopy (XPS).

Furthermore, Fourier-transform infrared (FTIR) spectroscopy, X-ray powder diffraction (XRD), and electrochemical impedance (EIS) characterization were conducted on all precursors following heating to $100\text{--}600^\circ\text{C}$, as phase and compositional changes are anticipated to influence materials’ processing methods and conductivities and shed light on potential applications for such materials as polymer and/or ceramic electrolytes.

RESULTS AND DISCUSSION

The syntheses of LiPON -like oligomer/polymer precursors start with phosphoramidate, $\text{OP}(\text{NH}_2)_3$. The simplest synthetic approach to $\text{OP}(\text{NH}_2)_3$ is via ammonolysis, reaction 1. However, it is difficult to remove byproduct NH_4Cl , which can interfere with purification depending on the solvent.^{46–49} The alternative is to use NaNH_2 per reaction 2. The higher solubility of LiCl vs NaCl in polar solvents can prevent simple precipitation, therefore NaNH_2 is preferable to LiNH_2 .



The design of LiPON -like oligomer/polymer precursor syntheses is presented in Scheme 1. For both Li_xPON and Li_xSiPON precursors, the syntheses start by reacting OPCl_3 with NaNH_2 or $(\text{Me}_3\text{Si})_2\text{NH}$, respectively (reaction sequences 3 and 4). On gently heating ($40^\circ\text{C}/1$ week) or reacting at room temperature (RT) for 1–2 weeks, the product forms an oligomeric/polymeric PON (SiPON) precursor. The byproduct NaCl in the Li_xPON system precipitates and is removed simply by filtration. The byproduct Me_3SiCl (bp = 57°C) is removed by vacuum evaporation at 40°C .

For Li_xSiPHN precursors, the first step is amination via silyl exchange between the phosphazene cyclomer $[\text{Cl}_2\text{P}=\text{N}]_3$ and $(\text{Me}_3\text{Si})_2\text{NH}$ obtaining SiPHN (synthesis sequence 5) coincident with the volatile byproduct Me_3SiCl .

Thereafter, all precursors can be lithiated using controlled amounts of LiNH_2 . The Li content in the LiPON -like precursors is readily controlled by the amount of LiNH_2 added, as confirmed by XPS studies below. In this work, the “ x ” in

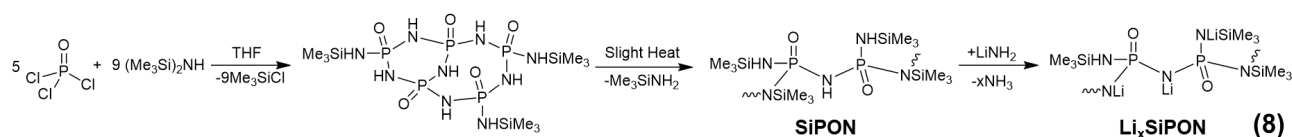
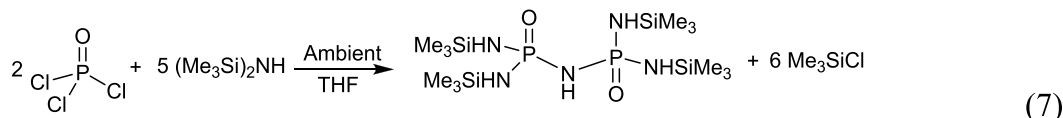
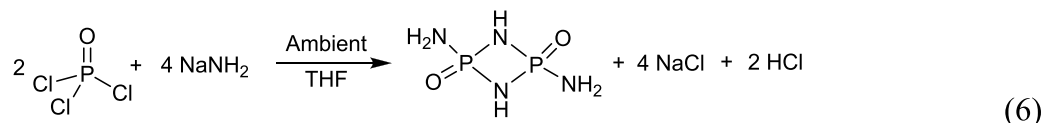
Scheme 2. Synthesis of Li_xSiPON Precursors with $(\text{Me}_3\text{Si})_2\text{NH}/\text{OPCl}_3 = 1.8:1$ 

Table 1. MWs and Estimated Compositions of Polymer Precursors

Polymer precursor	MW ^a , kDa	No. monomer units ^b	Possible monomer structures ^c
Li_3PON	0.6–1.4	5–15	
Li_6PON	0.6–1.9	5–20	
Li_2SiPHN	0.7–1.5	2–4	
Li_3SiPON	0.5–1.0	5–13	
Li_6SiPON	0.7–1.5	6–15	

^aMW = molecular weight. ^bNumber of monomer units calculated based on MALDI (Figures S2–S7 and Tables S1–S3). ^cIn the monomer structures, X = H or Li.

Li_xPON , Li_xSiPHN , and Li_xSiPON stands for the Li content based on the theoretical Li/P ratios used in the corresponding precursor syntheses.

One precursor design principle targets high ceramic yields (CYs) to minimize excessive volume changes associated with pyrolytic conversion of precursors (ave. precursor density ≈ 1) to ceramic materials (ave. density > 2.5).^{46–49,51} Higher CYs minimize pore formation from gaseous degradation products.

CYs typically improve with increases in molecular weight (MW).⁵¹ For Li_xPON and Li_xSiPON systems, one approach to promote polymerization is to reduce the ratio of NaNH_2 or $(\text{Me}_3\text{Si})_2\text{NH}$ to OPCl_3 prior to lithiation, as suggested by reactions 3 and 4. However, for the Li_xPON system, reducing the ratio of $\text{NaNH}_2/\text{OPCl}_3$ produces HCl (reaction 3), resulting in an acidic environment, which can be detrimental for lithiation and electrochemical performances.^{52,53}

In contrast, for the Li_xSiPON system, where no HCl is produced, a reduced $(\text{Me}_3\text{Si})_2\text{NH}/\text{OPCl}_3$ ratio of 1.8 is used, Scheme 2 (synthesis sequence 8). In this section, we characterize the reaction 3 derived Li_3PON and Li_6PON precursors. Similar results are presented for the Li_2SiPHN precursor from reaction 5 and Li_3SiPON and Li_6SiPON precursors from reaction 8.

Thus, Figure S1 shows representative GPCs of the lithium-free PON, SiPHN, and SiPON starting materials. The SiPHN and SiPON precursors show similar MWs of 0.2–2 kDa, while

PON shows MWs of ≤ 0.5 kDa. Both SiPHN and SiPON precursors are soluble in tetrahydrofuran (THF) forming clear solutions, while the PON precursor forms as a suspension. Since the GPC only analyzes soluble compounds, the actual MWs of the PON precursor are higher as demonstrated by MALDI-time-of-flight (ToF).

MALDI of the lithiated precursors and their possible monomer structures is given in Figures S2–S7. A computer program was developed to check all of the possible combinations, as given in the Supporting Information (SI). Negative-ion mode was used due to its higher resolution of LiPON-like precursors compared to the positive-ion mode. The ion source in negative-ion mode comes from the precursor itself, which loses one Li^+ . Tables S1–S3 list example calculations leading to the proposed structures representative of the precursors (Li_xPON , Li_xSiPHN , and Li_xSiPON). Table 1 summarizes MWs and estimated compositions of the polymer precursors based on GPC and MALDI studies. Note that the Li_2SiPHN precursor consists of monomers with higher individual MWs (300–600 g mol^{-1}) than those of Li_xPON (80–150 g mol^{-1}) and Li_xSiPON (80–220 g mol^{-1}) precursors, thus Li_2SiPHN oligomers have lower average numbers of monomer units than the other precursors despite MALDI spectra in similar mass ranges.

Figure S8 shows FTIR spectra of unlithiated PON, SiPHN, and SiPON precursors. Table S4 summarizes literature-reported

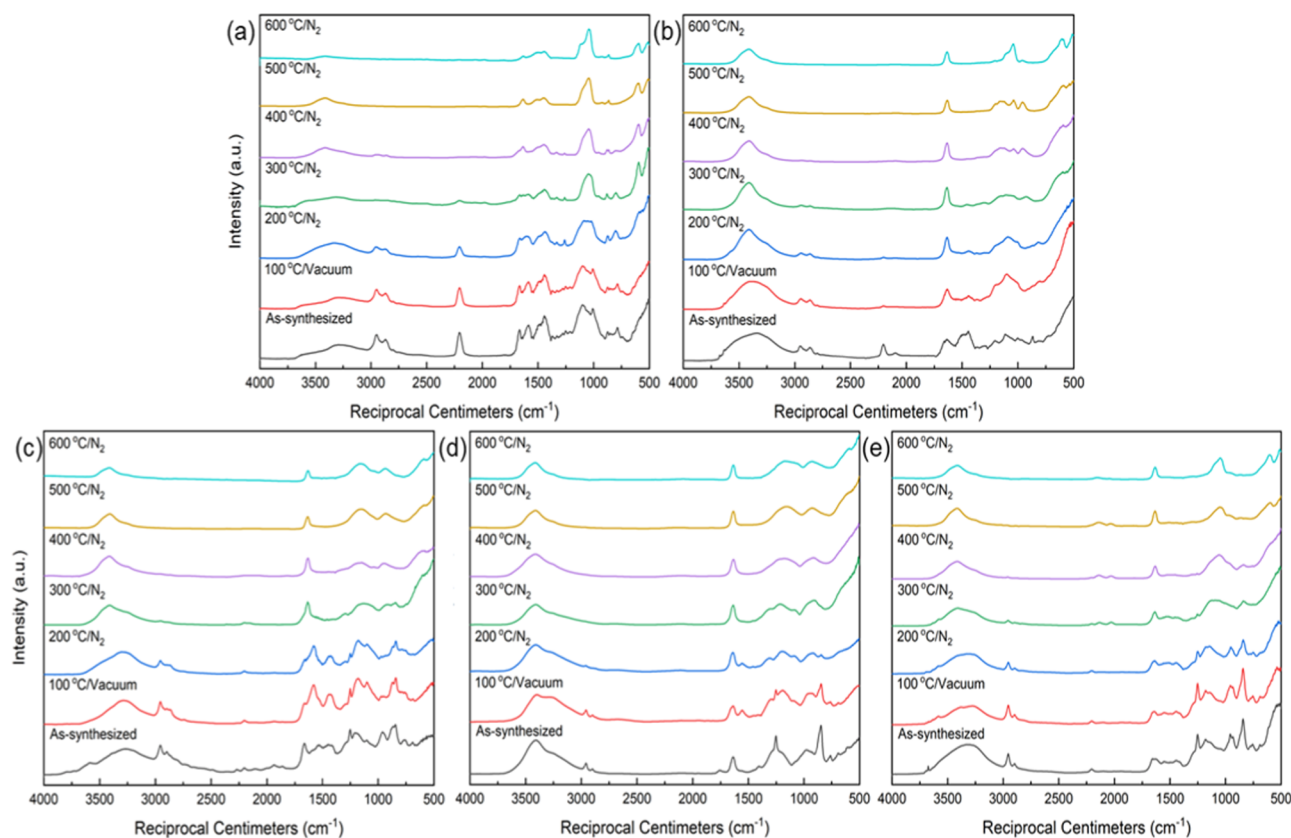


Figure 1. FTIR spectra of Li_3PON (a), Li_6PON (b), Li_2SiPHN (c), Li_3SiPON (d), and Li_6SiPON (e) precursors at different temperatures.

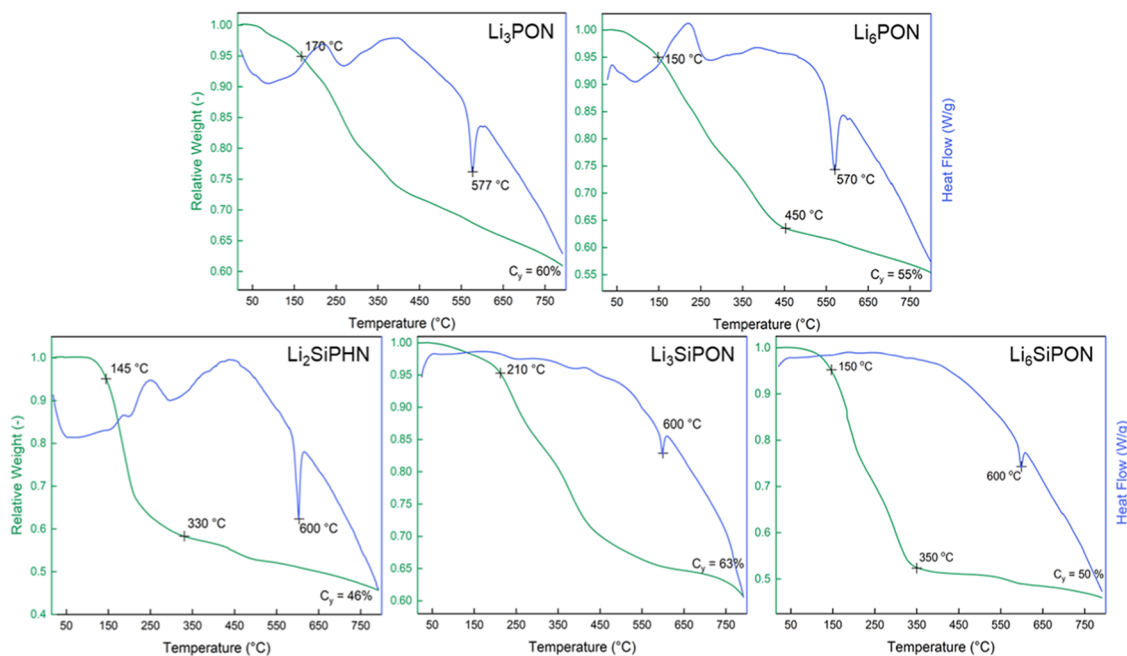


Figure 2. TGA–DTA (800 °C/10 °C min^{−1}/N₂) of Li_3PON , Li_6PON , Li_2SiPHN , Li_3SiPON , and Li_6SiPON precursors.

FTIRs of LiPON glasses. Typically, the unlithiated precursors exhibit $\nu\text{N-H}$ ($\sim 3000\text{ cm}^{-1}$) and N-H overtone ($\sim 1500\text{ cm}^{-1}$), $\nu\text{P=O}$ ($1150\text{--}1300\text{ cm}^{-1}$), $\nu\text{P-O}^-$ ($1000\text{--}1150\text{ cm}^{-1}$), and $\nu\text{P-N=P}$ ($800\text{--}900\text{ cm}^{-1}$) absorption bands.^{39,54–57} For the SiPHN precursor, since no oxygen is present, peaks at ~ 1200 and $970\text{--}850\text{ cm}^{-1}$ can be assigned to $\nu\text{P-N}$ and $\nu\text{P-N=P}$, respectively.^{39,55,57}

The lithiated precursors were heated to $100\text{--}600\text{ °C}$ (10 °C min^{-1}) under vacuum or N_2 ; Figure 1 shows the FTIR spectra of precursors at different temperatures (RT to 600 °C). In general, precursors below 200 °C show spectra similar to the unlithiated precursors, $\nu\text{N-H}$ (~ 3000 , $\sim 1500\text{ cm}^{-1}$), $\nu\text{P=O}$ ($1150\text{--}1300\text{ cm}^{-1}$), $\nu\text{P-O}^-$ ($1000\text{--}1150\text{ cm}^{-1}$), $\nu\text{P-N=P}$ ($800\text{--}900\text{ cm}^{-1}$), and $\nu\text{P-O-P}$ (1150 , $780\text{--}680\text{ cm}^{-1}$).^{39,54–57} Addition-

ally, Li_2SiPHN (Figure 1c) and Li_xSiPON (Figure 1d,e) precursors exhibit $\nu\text{C-H}$ at $\sim 2950\text{ cm}^{-1}$, which disappears at $\sim 300\text{ }^\circ\text{C}$. Often, we observe $\nu\text{O-H}$ at $\sim 3400\text{ cm}^{-1}$, possibly from excess LiNH_2 that reacts with trace moisture during sample preparation, forming LiOH .

In addition to the aforementioned adsorptions, a small peak at $\sim 2200\text{ cm}^{-1}$ is observed in some precursors, especially for the Li_3PON precursor. Pichonat et al.⁵⁷ and Stallworth et al.⁵⁸ suggest that peaks at $2200\text{--}2100\text{ cm}^{-1}$ may come from P-N^{P} or $\text{P-N}=\text{P}$ bonds. In general, the intensity of this peak decreases as temperature increases and disappears at $300\text{ }^\circ\text{C}$, suggesting rearrangement or reaction of these bonds. The intensities of $\nu\text{O-H/N-H}$ bonds reduce as temperatures increase; the dominant peak at $\sim 1040\text{ cm}^{-1}$ and at $600\text{ }^\circ\text{C}$ can be assigned to $\nu\text{P-O}^-$.^{59,60}

Figure 2 compares representative TGA–DTA ($800\text{ }^\circ\text{C}/10\text{ }^\circ\text{C min}^{-1}/\text{N}_2$) of the vacuum-dried ($100\text{ }^\circ\text{C}/1\text{ h}$) precursors (Li_xPON , Li_xSiPHN , and Li_xSiPON). All precursors typically have 5% mass loss temperatures ($T_{5\%}$) $\geq 150\text{ }^\circ\text{C}$ and similar ceramic yields (CYs) of 50–60 wt % at $800\text{ }^\circ\text{C}$. An endotherm at $\sim 600\text{ }^\circ\text{C}$ is exhibited for all of the precursors, which suggests melting. This provides the potential of melt bonding for solid-state battery assembly.

Figure 3 compares ^7Li NMR (CDCl_3) of vacuum-dried (RT) polymer precursors; the bandwidth of Li_xSiPON precursors is

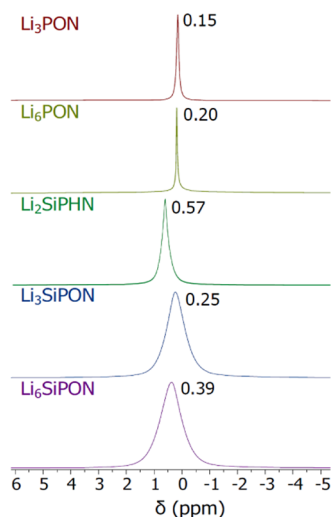


Figure 3. ^7Li NMR of Li_3PON , Li_6PON , Li_2SiPHN , Li_3SiPON , and Li_6SiPON precursors (RT/vacuum-dried, dissolved in CDCl_3).

qualitatively greater than that found for the Li_xPON and Li_2SiPHN precursors, suggesting that these precursors may have several Li^+ chemical environments.

Based on the above-proposed precursor structures, one can suggest possible Li^+ environments per Figure 4. If we consider Li^+ bonded to a N of $(\text{H})\text{N-P}$ as type A, typical for Li_xPON

(marked as red in Figure 4), and Li^+ bonded to a N between SiMe_3 and P as type B, typical for Li_xSiPHN (marked as green in Figure 4), then Li_xSiPON precursors will have both types in agreement with the ^7Li NMRs for both Li_xPON and Li_2SiPHN precursors, which show single sharp peaks at different chemical shifts. In contrast, the Li_xSiPON precursors show broader peaks with chemical shifts similar to Li_2SiPHN due to the presence of SiMe_3 groups.

Of import, precursors with higher Li^+ contents also seem to show higher chemical shifts ($\text{Li}_6\text{PON} > \text{Li}_3\text{PON}$ and $\text{Li}_6\text{SiPON} > \text{Li}_3\text{SiPON}$) in agreement with See et al.,⁶¹ using a mixture of dioxolane and dimethoxyethane (DOL/DME, 1:1). This group found that ^7Li resonances shift to higher frequencies with increases in Li^+ concentration. These results may derive from increased numbers of solvated Li^+ ions, causing a deshielding effect but may also be due to changes in the Li^+ coordination number.

Table S5 lists ^7Li NMR studies of various compounds in solution from the literature. Typically, a standard reference (0.1 or 1 M LiCl in D_2O or THF-d_8) is used. In general, Li^+ in a complex structure with considerable electron shielding shows upfield chemical shifts. In contrast, Li^+ cations in the LiClO_4 solution are highly dissociated and show a large downfield chemical shift (2.12 ppm). The positive chemical shifts found for the Li_xPON , LiSiPHN , and Li_xSiPON precursors suggest that the Li^+ ions are well solvated and dissociated, which is in accord with our findings that they offer superior properties in a set polymer electrolyte batteries with Li-S cathodes and as ceramic precursors on ceramic electrolytes.^{50,62}

Additionally, N/P ratios may also influence chemical shifts (Table 2). As suggested by Muñoz et al.,⁶³ higher nitrogen

Table 2. ^7Li NMR and Atomic Ratios Based on XPS Analyses for Polymer Precursors (RT/Vacuum-Dried)

	Li_3PON	Li_6PON	Li_2SiPHN	Li_3SiPON	Li_6SiPON
^7Li NMR (ppm)	0.15	0.20	0.57	0.25	0.39
O/P	4.6	4.8	1.3	1.7	3.0
N/P	1.1	1.4	3.0	1.9	2.0
Li/N	1.0	2.0	0.3	0.95	1.4
Li/P	1.1	2.7	0.9	1.8	2.8

The bold values indicate correlations between N/P ratios and ^7Li chemical shifts.

contents (N/P ratios) lead to increases in the chemical shifts of the ^7Li NMR resonances, related to decreases in average Li^+ coordination numbers.^{63,64}

Figure 5a shows ^{13}C NMRs of Li_2SiPHN and Li_xSiPON precursors (C-containing precursors). All precursors exhibit a peak at $\sim 2.5\text{ ppm}$ similar to $(\text{Me}_3\text{Si})_2\text{NH}$ ($\delta_{\text{C}} = 2.64\text{ ppm}$), corresponding to carbons in the NH-SiMe_3 groups. However, this peak is slightly shifted upfield ($\Delta\delta = 0.10\text{--}0.15\text{ ppm}$). NMR chemical shifts are affected by electron density, when



Figure 4. Exemplary structures of Li_xPON , Li_xSiPHN , and Li_xSiPON precursors with Li^+ highlighted.

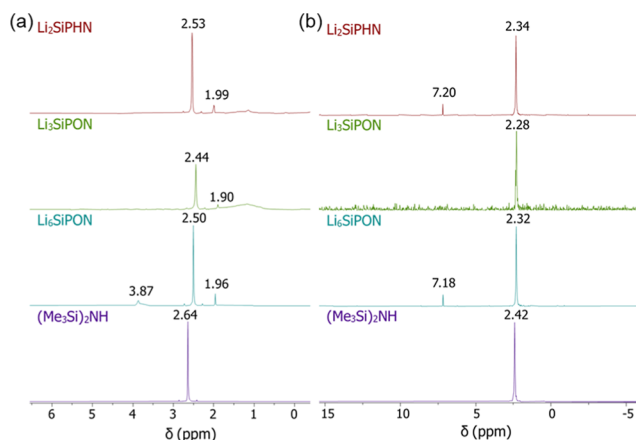


Figure 5. ^{13}C NMR (a) and ^{29}Si NMR (b) of Li_2SiPHN , Li_3SiPON , and Li_6SiPON precursors (RT/vacuum-dried, dissolved in CDCl_3) in comparison with $(\text{Me}_3\text{Si})_2\text{NH}$.

$(\text{Me}_3\text{Si})_2\text{NH}$ loses one SiMe_3 and bonds with $\text{P}=\text{O}$ or $\text{P}=\text{N}=\text{P}$ (see the examples in Figure 4) in the polymer backbone; the carbon environment changes slightly (more shielded), causing a $\Delta\delta \approx 0.2$ ppm upfield shift.

Additionally, a small peak at ~ 2 ppm is exhibited in all precursors, which may be the $\text{Me}_3\text{SiO}-$ group. As shown in Figure S9a, $(\text{Me}_3\text{Si})_2\text{O}$ has a δ_c of 1.94 ppm.

Some precursors also show a small peak at ~ 3.9 ppm, which may be Me_3SiCl or Me_3SiNH_2 . As shown in Figure S9b, Me_3SiCl has a δ_c of 3.26 ppm,⁶⁵ slightly different from our observation. Therefore, the peak at ~ 3.9 ppm is likely Me_3SiNH_2 (NMR spectrum not found in the literature).

Figure 5b shows ^{29}Si NMRs of silicon-containing polymer precursors. All precursors show a peak at 2.3 ppm corresponding to $\text{NH}-\text{SiMe}_3$ groups, similar to the chemical shift of $(\text{Me}_3\text{Si})_2\text{NH}$ at 2.42 ppm. In accordance with ^{13}C NMR, the upfield shift ($\Delta\delta \approx 0.1$ ppm) suggests that the silicon environment becomes more shielded when $(\text{Me}_3\text{Si})_2\text{NH}$ loses one $-\text{SiMe}_3$ and bonds to the polymer backbone.

Some precursors also show a smaller peak at 7.2 ppm, which may be Me_3SiNH_2 or Me_3SiCl , as the silicon would be less electronically shielded (lower electron density near H and higher electronegativity with Cl) compared to $\text{P}=\text{O}-\text{NH}-(\text{SiMe}_3)_2$ or $\text{P}=\text{N}=\text{P}-\text{NH}(\text{SiMe}_3)_2$. Table S6 shows the electronegativity of the selected elements. However, Me_3SiCl has a δ_{Si} of 31 ppm.^{65,66} Therefore, the corresponding compound at 7.2 ppm is likely Me_3SiNH_2 , which is in agreement with the δ_c at 3.9 ppm for the ^{13}C NMR study.

Due to the lower sensitivity of ^{29}Si NMR, fewer peaks are observed compared to ^{13}C NMR.

Figure 6 shows the ^1H NMRs of proton-containing polymer precursors and $(\text{Me}_3\text{Si})_2\text{NH}$. In general, protons from methyl groups and THF are observed. Since the precursors are dried at room temperature, there is a trace amount of THF left. All precursors show a large peak at 0.01 ppm, which is similar to the $-\text{CH}_3$ groups from $(\text{Me}_3\text{Si})_2\text{NH}$ at 0.06 ppm, but slightly shifted to upfield, likely a result of polymerization causing a shielding effect in agreement with ^{13}C and ^{29}Si NMR studies.

Additionally, small peaks at 0.15–0.2 ppm are exhibited. Figure S10 shows ^1H NMR models of Me_3SiNH_2 , $(\text{Me}_3\text{Si})_2\text{O}$, and Me_3SiCl by ChemDraw, the main δ_{H} are 0.08, 0.21, and 0.42 ppm, respectively. The chemical shift at 0.15–0.2 ppm may be $\text{Me}_3\text{SiO}-$ groups that shifted upfield due to interactions with the polymer precursors.

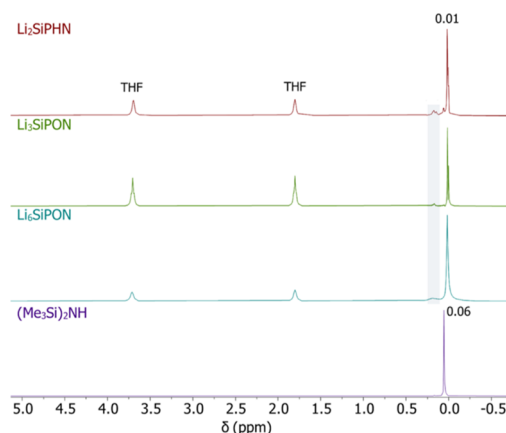


Figure 6. ^1H NMR of Li_2SiPHN , Li_3SiPON , and Li_6SiPON precursors (RT/vacuum-dried, dissolved in CDCl_3) in comparison with $(\text{Me}_3\text{Si})_2\text{NH}$.

Overall, only $-\text{SiMe}_3$ protons are observed, and no proton migration is suggested by ^1H NMR.

Figures 7 and S11a show XRD patterns of Li_xPON pellets heated to 100–600 $^\circ\text{C}/2$ h/ N_2 . The XRD of Li_3PON pellets

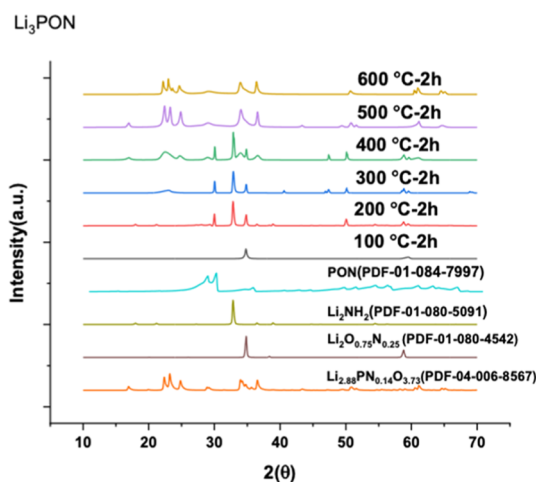


Figure 7. XRD plots of Li_3PON pellets heated to 100–600 $^\circ\text{C}/2$ h/ N_2 .

heated to 100 $^\circ\text{C}$ shows a small peak near $35^\circ 2\theta$, corresponding to the $\text{Li}_2\text{O}_{0.75}\text{N}_{0.25}$ phase (PDF-01-080-4542) with space group $225: Fm\bar{3}m$. However, the spectrum is dominated by a broad peak at $20^\circ 2\theta$ corresponding to the amorphous nature of the material. Three peaks at 30, 33, and $35^\circ 2\theta$ can be indexed to partially crystalline $\text{Li}_{2.88}\text{PN}_{0.14}\text{O}_{3.73}$, Li_2NH_2 , and $\text{Li}_2\text{O}_{0.75}\text{N}_{0.25}$ phases, respectively, when the pellet is heated to 200–400 $^\circ\text{C}$. These peaks shift to 35 and $37^\circ 2\theta$ along with additional doublet peaks near $23^\circ 2\theta$ when the pellet is heated to 500 and 600 $^\circ\text{C}$ corresponding to $\text{Li}_{2.88}\text{PN}_{0.14}\text{O}_{3.73}$. Similar peaks are present for Li_6PON pellets, as shown in Figure S11.

Figures 8 and S11c show XRD patterns for Li_xSiPON pellets heated to 100–600 $^\circ\text{C}/2$ h/ N_2 . The XRD of Li_3SiPON pellets heated to 100–300 $^\circ\text{C}$ is dominated by a broad peak corresponding to a poorly crystallized material, indicating an amorphous nature. Two main peaks at 22 and $29^\circ 2\theta$ can be indexed to partially crystalline $\text{Li}_4\text{P}_2\text{O}_7$ (PDF-01-084-7598) after heating to 400 and 500 $^\circ\text{C}$. The single peak $\sim 29^\circ 2\theta$ starts to split into double peaks when the pellet is heated above 500 $^\circ\text{C}$. The XRD of Li_3SiPON pellets heated to 600 $^\circ\text{C}$ shows sharp

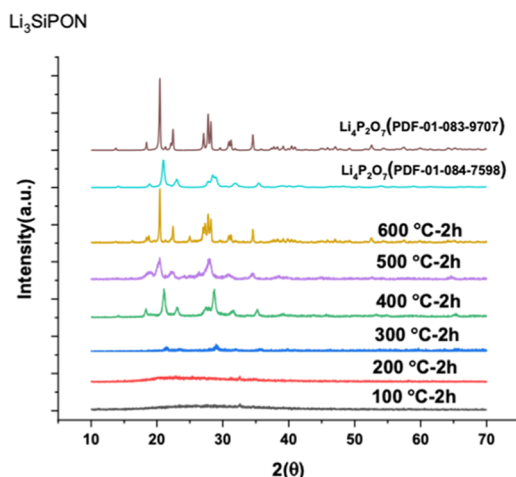


Figure 8. XRD plots of the Li_3SiPON pellet heated to 100–600 °C/2 h/ N_2 .

peaks matching $\text{Li}_4\text{P}_2\text{O}_7$ (PDF-01-083-9707), indicating a loss of nitrogen doping.

Figure S11c shows that the XRD of Li_6SiPON pellets heated to 100 and 200 °C is mostly dominated by a broad peak. The pellet heated to 300 °C showed doublet peaks ~ 20 and $30^\circ 2\theta$ indexed to partially crystalline Li_3PO_4 . The XRD of Li_6SiPON pellets heated to 400–600 °C shows sharp peaks matching Li_3PO_4 (PDF-04-007-2815), indicating a loss of nitrogen doping.

XRD studies at 100 °C showed mainly an amorphous phase, and hence, this technique can neither detect the targeted elements nor quantify the components and/or elemental ratios. Hence, XPS studies were run on Li_3PON , Li_6PON , Li_2SiPHN , Li_3SiPON , and Li_6SiPON precursors dried under vacuum for 3 d/RT. Dried precursor (0.5 g) powders were pelletized using 13 mm diameter die/5 ksi/RT. The data are presented in Figure 9.

Figure 9a,b shows wide-scan XPS survey spectra of Li_3PON and Li_6PON pellets, which provide elemental compositions of Li_3PON and Li_6PON pellets, confirming the signature elements, with minor peaks for C and Cl. The presence of chlorine likely arises from residual NaCl. Carbon is ubiquitous in XPS spectra but also may reflect brief exposure of the precursor to air forming Li_2CO_3 during pelletization. The results obtained from XPS are summarized in Tables S7 and 2. They confirm the presence and incorporation of nitrogen into the pellets and reinforce the fact that the chemical makeup of the Li_3PON and Li_6PON pellets is similar to that found in previous studies of gas-phase deposited materials.^{21,57,67}

The deduced atomic composition shows that the Li atom % increased from ~ 7 to 12.6 when LiNH_2 was doubled from Li_3PON to Li_6PON . Moreover, XPS analysis also provides information about bonding environments. The O 1s peak is attributed to Li–O–Li, P–O–P, and P=O bonds. The N/P ratio (1.1–1.4) is higher than what is reported by gas-phase deposition techniques (0.92), which seems to be reflected in the higher Li^+ conductivities seen in the materials prepared here.⁵⁷

In Figure 9d,e, wide-scan survey XPS spectra of Li_3SiPON and Li_6SiPON pellets also present representative LiSiPON elemental signatures and minor peaks for C and Cl. The presence of chlorine might be from residual NaCl or ClSiMe_3 . The presence of carbon can arise as noted above or from $\text{NH}(\text{SiMe}_3)_2$. The XPS results are summarized in Tables S8 and 2.

The deduced atomic compositions show that the Li atom % increased from ~ 13 to 18 when more LiNH_2 is introduced in synthesizing Li_6SiPON . In addition, the Li content is higher than that calculated for Li_3PON (7) and Li_6PON (12.6) pellets. This may be due to incorporation of silicon in the polymer precursor. It has been reported that partial substitution of P by Si in LiPO_4 results in an increase in Li^+ mobility by shortening the distance between adjacent positions for Li^+ hopping.⁶⁸

Furthermore, it has also been demonstrated that increases in N in LiSiPON films increase the conductivity. The increase in

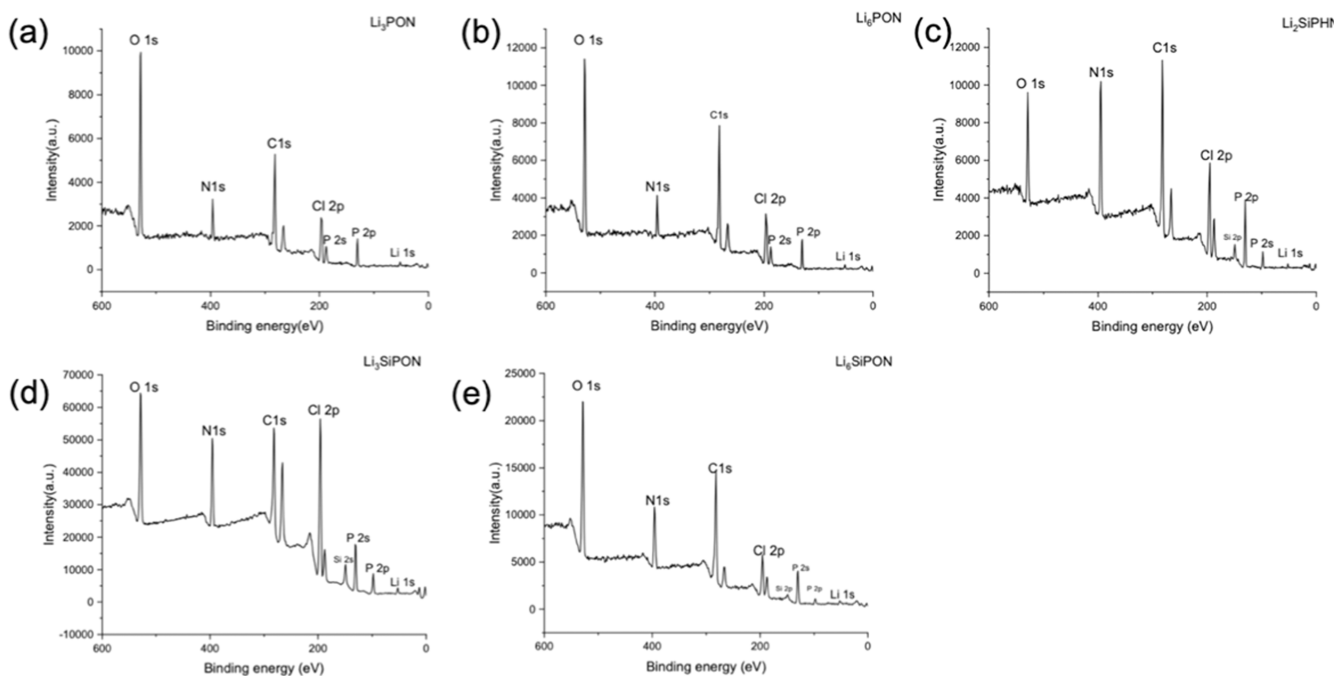


Figure 9. Wide-scan survey XPS spectra (600–0 eV) of Li_3PON (a), Li_6PON (b), Li_2SiPHN (c), Li_3SiPON (d), and Li_6SiPON (e) pellets (RT/vacuum-dried).

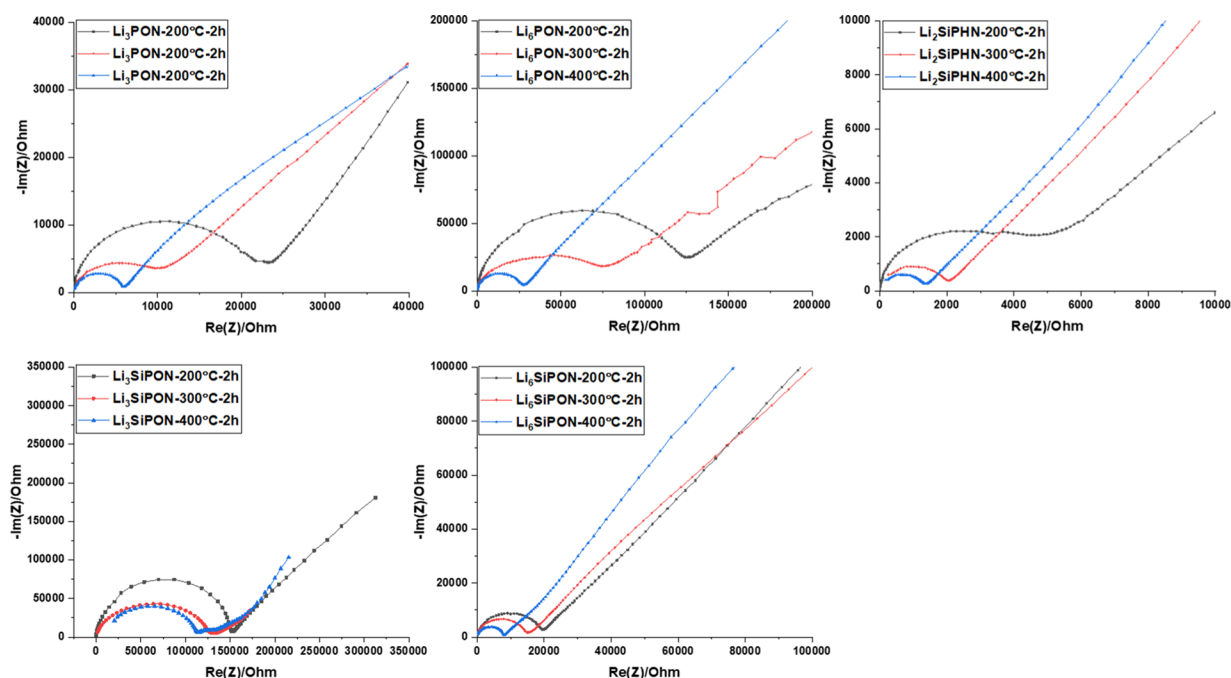


Figure 10. Nyquist plots of polymer precursor pellets heated to 200, 300, and 400 °C/2 h/N₂.

the Si/P ratio has been hypothesized to improve the N content.³² The experimental ratio of N/P was calculated to be 3; the decrease in the ratio from XPS points to polymerization by a loss of nitrogen. However, the N/P ratio (~ 2) is still higher than that for Li₃PON and Li₆PON in Table 2. The Li₆SiPON polymer electrolyte also shows the lowest Cl atom %.

In Figure 9c, wide-scan survey XPS of Li₂SiPHN presents the expected elemental signatures and minor peaks for C and Cl. The latter elements are likely sourced as noted above. The results obtained from XPS are summarized in Tables S9 and 2.

The calculated atomic composition shows a Li/P ratio of 0.9, as listed in Table 2. However, this ratio is smaller than what is calculated experimentally for Li₂SiPHN; the discrepancies are thought to arise from polymerization that reduces the number of sites that can be lithiated. Another explanation might be due to the fact that XPS can only be used to predict the composition of thin films and not bulk pellets.

Scanning electron microscopy (SEM) and energy-dispersive X-ray (EDX) studies were conducted to characterize the microstructures and the composition of the polymer precursors. Figures S12 and S13 show SEM fracture surface images of Li₃PON, Li₆PON, Li₂SiPHN, Li₃SiPON, and Li₆SiPON precursor pellets heated to 100–400 °C/2 h/N₂. The pellets heated to 100 °C, in general, show a very smooth, uniform, and dense microstructure. This might be ascribed to the fact that these precursors show a very small mass loss before 200 °C, as demonstrated by the TGA–DTA in Figure 2. The pellets heated between 200 and 300 °C present a three-dimensional (3D) network of structures forming microglobules. On heating to 400 °C, the pellets present a porous microstructure ascribed to the loss of volatiles and organic compounds indicating the ceramization of the precursors, as supported by the XRD in Figures 7 and 8.

Figures S14 and S15 show EDX map images of polymer precursor pellets heated to 100 °C/2 h/N₂. The EDX map shows well-distributed signature elements (N, O, P, and Si) and indicates the presence of impurities such as Cl from the starting

material and C from Li₂CO₃ in good agreement with the XPS data shown in Figure 9. The qualitative EDX results are summarized in Tables S10 and S11. The N/P ratio seems to increase with the heating temperature of the polymer precursor pellets, which might be ascribed to the loss of CO₂ during heating. The Li₆PON pellets showed a lower N/P ratio compared to Li₃PON, resulting in a lower ionic conductivity in the Li₆PON pellets.

Li⁺ Conductivity Measurements. Conductivity measurements were run on compacted pellets rather than thin films, as reported in complementary manuscripts.^{50,62} Li₃PON, Li₆PON, Li₂SiPHN, Li₃SiPON, and Li₆SiPON precursors were heated to 100 °C/vacuum/24 h. The dried polymer precursor (3 g) powder was compacted as above. The resulting pellets were heated between alumina plates to 100–400 °C/2 h at 1 °C min^{−1} under 120 mL min^{−1} N₂ flow. Concentric Au/Pd electrodes (3 mm in diameter) were deposited using an SPI sputter coater on both the surfaces of the pellets using a deposition mask. An equivalent circuit consisting of ($R_{\text{total}}Q_{\text{total}}$)-($Q_{\text{electrode}}$) was used. R and Q denote resistance and constant phase elements, respectively. The total conductivity (σ_t) was calculated using the equation ($\sigma_t = t/(A \times R)$), where t is the thickness of the polymer precursor pellet, A is the active area of the polymer precursor, and R is the total resistivity obtained from the Nyquist plots.

Figure 10 shows Nyquist plots of Li₃PON, Li₆PON, Li₂SiPHN, Li₃SiPON, and Li₆SiPON pellets heated to 200–400 °C/2 h/N₂. All of the measurements were conducted at room temperature.

Table 3 summarizes the total conductivity of the polymer precursor pellets heated to 200–400 °C/2 h/N₂. The highest conductivities are obtained on heating to 400 °C. The conductivity seems to improve with increasing temperature, improving pathways for Li⁺ diffusion due to phase change, as demonstrated by XRD plots in Figures 7 and 8. Li₂SiPHN shows the highest conductivity of 3×10^{-1} mS cm^{−1} at 400 °C. This polymer precursor also showed the densest microstructure when

Table 3. Total Conductivities (σ_{RT}) of Polymer Precursor Pellets Heated to 200–400 °C/2 h/ N_2

polymer pellets	temp. (°C)	σ_{RT} (S cm ⁻¹)
Li ₃ PON	200/2 h	1.1×10^{-5}
	300/2 h	1.8×10^{-5}
	400/2 h	4.5×10^{-5}
Li ₆ PON	200/2 h	1.9×10^{-6}
	300/2 h	5.3×10^{-6}
	400/2 h	1.2×10^{-5}
Li ₂ SiPHN	200/2 h	5.7×10^{-5}
	300/2 h	1.5×10^{-4}
	400/2 h	2.7×10^{-4}
Li ₃ SiPON	200/2 h	2.0×10^{-6}
	300/2 h	1.6×10^{-6}
	400/2 h	4.0×10^{-6}
Li ₆ SiPON	200/2 h	1.9×10^{-5}
	300/2 h	2.0×10^{-5}
	400/2 h	3.3×10^{-5}

compared to the Li_xSiPON polymer precursors. The Li₃SiPON showed the lowest conductivity when heated to 400 °C ascribed to the increased porosity in the microstructure, as shown in Figure S13. The Li_xPON polymer precursors showed poor ionic conductivity compared to the Si-based polymer precursors. These phenomena can be explained by the low N/P ratios (<1.5) as well as the poor microstructure, as shown in Figures 9 and S12, respectively.

CONCLUSIONS

In summary, we present here a detailed characterization of LiPON-like oligomer/polymer precursors, including MALDI, FTIR, TGA–DTA, NMR, XRD, XPS, and impedance studies. For all of the precursors, the MWs are estimated to be ≈ 1 –2 kDa, and the CYs at 800 °C are 50–60%. They are thermally stable to 150–200 °C. FTIR spectra fit well with typical LiPON glasses synthesized by gas-phase methods.^{39,54–58} ⁷Li NMR suggests that Li⁺ ions in these precursors are well solvated and dissociated, which is beneficial for their electrochemical performances. The structures of Si (C)-containing precursors were further investigated by ¹³C and ²⁹Si NMR studies, which suggests that Si doping was achieved by bonding NH–SiMe₃ with P=O or P–N=P onto the polymer backbone.

Crystalline phases of these polymer precursors at different temperatures (100–600 °C) were characterized by XRD. However, they are primarily amorphous at 100 °C, and hence, XPS and EDX studies were performed to quantify the elemental composition of the precursors. Overall, all of the precursors show higher N/P ratios (1–3) compared to traditional gas-phase methods (<1), and there seems to be a correlation between the N/P ratio and ⁷Li NMR chemical shift. All of the polymer precursors show the highest room temperature conductivity after treating at 400 °C/2 h. In general, the conductivities of polymer precursor pellets seem to be Li₂SiPHN \gg Li₆SiPON \gg Li₃PON \gg Li₆PON \gg Li₃SiPON.

EXPERIMENTAL SECTION

Materials. Phosphorus oxychloride (OPCl₃) and hexamethyldisilazane [NH(SiMe₃)₂] were obtained from Alfa Aesar. Sodium amide (NaNH₂) and lithium amide (LiNH₂) were obtained from Acros Organics. Hexachlorophosphazene (Cl₆N₃P₃) was purchased from abcr GmbH. All chemicals were used as received. All reactions were conducted under a N₂ atmosphere.

Polymer Precursor Syntheses. The polymer precursors are synthesized in two steps. The first step is to substitute the –Cl in the phosphorus source (OPCl₃ or Cl₆N₃P₃) with –NH₂ (from NaNH₂) or –NHSiMe₃ [from NH(SiMe₃)₂], producing byproduct NaCl or Me₃SiCl (Table S12). It is followed by lithiation from the lithium source LiNH₂.

Typical Synthesis Procedures. In a dried 200 mL round-bottom Schlenk flask, NaNH₂ (7.0 g, 0.179 mol) or (Me₃Si)₃NH (20.1 mL, 96.6 mmol) was first added to 80 mL of distilled THF, then OPCl₃ (5.0 mL, 53.6 mmol) or Cl₆N₃P₃ (5.2 g, 14.9 mmol) was added. All were done in an ice bath under a N₂ atmosphere. The ice bath was removed after 1 day of reaction, and the reaction was kept running at room temperature (RT) under the N₂ atmosphere for 1 week. Centrifugation was followed to separate the soluble and insoluble parts in the reaction mixture. The supernatant was collected into another dried 200 mL round-bottom Schlenk flask.

Thereafter, LiNH₂ (see Table S13) was added to the supernatant under the N₂ atmosphere in an ice bath. The reaction mixture stayed cloudy due to the low solubility of LiNH₂. After 1 day of reaction, the ice bath was removed and changed to an oil bath for heating. The reaction was kept running at 40 °C under the N₂ atmosphere for a week. Centrifugation was followed to separate the soluble and insoluble parts in the reaction mixture. The supernatant was collected into another dried 200 mL round-bottom Schlenk flask.

To obtain the yield, a small sample (3 mL) was taken from the centrifuged supernatant and vacuum-dried at 60 °C on a Schlenk line and the mass of the product was measured. The total volume of the supernatant was measured by a graduated pipette.

Table S13 lists the LiNH₂ used in the lithiation and the properties of the final products.

ASSOCIATED CONTENT

Supporting Information

The Supporting Information is available free of charge at <https://pubs.acs.org/doi/10.1021/acs.macromol.0c00254>.

Analytical methods and data; GPC of unlithiated PON, SiPHN, and SiPON precursors; negative-ion mode MALDI; monomer structures and compositions of Li_xPON, Li₂SiPHN, and Li_xSiPON precursors; FTIR spectra; ⁷Li NMR and ¹³C NMR studies; electronegativity of selected elements; ¹H NMR models; XRD plots and analysis; SEM and EDX images; atomic ratios based on EDX analyses; P, N source and the stoichiometry; lithiation of the polymer precursors. Python program for polymer structure calculations based on MALDI-ToF (PDF)

AUTHOR INFORMATION

Corresponding Author

Richard M. Laine – Department of Materials Science and Engineering, University of Michigan, Ann Arbor, Michigan 48109-2136, United States; orcid.org/0000-0003-4939-3514; Email: talsdad@umich.edu

Authors

Xinyu Zhang – Department of Materials Science and Engineering, University of Michigan, Ann Arbor, Michigan 48109-2136, United States

Eleni Temeche – Department of Materials Science and Engineering, University of Michigan, Ann Arbor, Michigan 48109-2136, United States

Complete contact information is available at:

<https://pubs.acs.org/doi/10.1021/acs.macromol.0c00254>

Author Contributions

The manuscript was written through contributions of all authors. All authors have given approval to the final version of the manuscript.

Notes

The authors declare no competing financial interest.

ACKNOWLEDGMENTS

We are grateful for the support of a significant portion of this work by DOE through Batt500 Seedling project DE-EE0008235 and a gift from Daimler Mercedes. A portion of this work was also supported by a DMR NSF Grant No. DMR 099217. We also thank the University of Michigan Energy Institute (UMEI) and Michigan Translational Research and Commercialization (MTRAC) program for support of the purchase chemicals, solvents, furnace, and LF-FSP reactor components. We especially thank Tobias Glossman and Prof. Dr. Andreas Hintennach of Mercedes-Daimler for their encouragement. We also thank Andrew Alexander for his assistance in providing the computer program for polymer precursor structure calculations based on MALDI-ToF.

REFERENCES

- (1) Put, B.; Vereecken, P. M.; Meersschaet, J.; Sepúlveda, A.; Stesmans, A. Electrical Characterization of Ultrathin RF-Sputtered LiPON Layers for Nanoscale Batteries. *ACS Appl. Mater. Interfaces* **2016**, *8*, 7060–7069.
- (2) Oudenhoven, J. F. M.; Baggetto, L.; Notten, P. H. L. All-Solid-State Lithium-Ion Microbatteries: A Review of Various Three-Dimensional Concepts. *Adv. Energy Mater.* **2011**, *1*, 10–33.
- (3) Patil, A.; Patil, V.; Wook Shin, D.; Choi, J. W.; Paik, D. S.; Yoon, S. J. Issue and Challenges Facing Rechargeable Thin Film Lithium Batteries. *Mater. Res. Bull.* **2008**, *43*, 1913–1942.
- (4) Long, J. W.; Dunn, B.; Rolison, D. R.; White, H. S. Three-Dimensional Battery Architectures. *Chem. Rev.* **2004**, *104*, 4463–4492.
- (5) Rolison, D. R.; Long, J. W.; Lytle, J. C.; Fischer, A. E.; Rhodes, C. P.; McEvoy, T. M.; Bourg, M. E.; Lubers, A. M. Multifunctional 3D Nanoarchitectures for Energy Storage and Conversion. *Chem. Soc. Rev.* **2009**, *38*, 226–252.
- (6) Hartmann, P.; Leichtweiss, T.; Busche, M. R.; Schneider, M.; Reich, M.; Sann, J.; Adelhelm, P.; Janek, J. Degradation of NASICON-Type Materials in Contact with Lithium Metal: Formation of Mixed Conducting Interphases (MCI) on Solid Electrolytes. *J. Phys. Chem. C* **2013**, *117*, 21064–21074.
- (7) Manthiram, A.; Yu, X.; Wang, S. Lithium Battery Chemistries Enabled by Solid-State Electrolytes. *Nat. Rev. Mater.* **2017**, *2*, No. 16103.
- (8) Pitawala, H. M. J. C.; Dissanayake, M. A. K. L.; Seneviratne, V. A.; Mellander, B. E.; Albinson, I. Effect of Plasticizers (EC or PC) on the Ionic Conductivity and Thermal Properties of the (PEO) 9LiTf: Al 2O 3 Nanocomposite Polymer Electrolyte System. *J. Solid State Electrochem.* **2008**, *12*, 783–789.
- (9) Imanishi, N.; Hasegawa, S.; Zhang, T.; Hirano, A.; Takeda, Y.; Yamamoto, O. Lithium Anode for Lithium-Air Secondary Batteries. *J. Power Sources* **2008**, *185*, 1392–1397.
- (10) Yu, X.; Bi, Z.; Zhao, F.; Manthiram, A. Polysulfide-Shuttle Control in Lithium-Sulfur Batteries with a Chemically/Electrochemically Compatible NaSICON-Type Solid Electrolyte. *Adv. Energy Mater.* **2016**, *6*, No. 1601392.
- (11) Wu, B.; Wang, S.; Lochala, J.; Desrochers, D.; Liu, B.; Zhang, W.; Yang, J.; Xiao, J. The Role of the Solid Electrolyte Interphase Layer in Preventing Li Dendrite Growth in Solid-State Batteries. *Energy Environ. Sci.* **2018**, *11*, 1803–1810.
- (12) Cheng, E. J.; Sharafi, A.; Sakamoto, J. Intergranular Li Metal Propagation through Polycrystalline Li_{6.25}Al_{0.25}La₃Zr₂O₁₂ Ceramic Electrolyte. *Electrochim. Acta* **2017**, *223*, 85–91.
- (13) Sharafi, A.; Meyer, H. M.; Nanda, J.; Wolfenstine, J.; Sakamoto, J. Characterizing the Li-Li₇La₃Zr₂O₁₂ Interface Stability and Kinetics as a Function of Temperature and Current Density. *J. Power Sources* **2016**, *302*, 135–139.
- (14) Li, G.; Monroe, C. W. Dendrite Nucleation in Lithium-Conductive Ceramics. *Phys. Chem. Chem. Phys.* **2019**, *21*, 20354–20359.
- (15) Yu, S.; Siegel, D. J. Grain Boundary Contributions to Li-Ion Transport in the Solid Electrolyte Li₇La₃Zr₂O₁₂ (LLZO). *Chem. Mater.* **2017**, *29*, 9639–9647.
- (16) Tian, H. K.; Xu, B.; Qi, Y. Computational Study of Lithium Nucleation Tendency in Li₇La₃Zr₂O₁₂ (LLZO) and Rational Design of Interlayer Materials to Prevent Lithium Dendrites. *J. Power Sources* **2018**, *392*, 79–86.
- (17) Lin, C. F.; Fan, X.; Pearce, A.; Liou, S. C.; Gregorczyk, K.; Leskes, M.; Wang, C.; Lee, S. B.; Rubloff, G. W.; Noked, M. Highly Reversible Conversion-Type FeOF Composite Electrode with Extended Lithium Insertion by Atomic Layer Deposition LiPON Protection. *Chem. Mater.* **2017**, *29*, 8780–8791.
- (18) Lin, C. F.; Qi, Y.; Gregorczyk, K.; Lee, S. B.; Rubloff, G. W. Nanoscale Protection Layers to Mitigate Degradation in High-Energy Electrochemical Energy Storage Systems. *Acc. Chem. Res.* **2018**, *51*, 97–106.
- (19) Westover, A. S.; Dudney, N. J.; Sacchi, R. L.; Kalnaus, S. Deposition and Confinement of Li Metal along an Artificial Lipon-Lipon Interface. *ACS Energy Lett.* **2019**, *4*, 651–655.
- (20) Yu, X.; Bates, J. B.; Jellison, G. E.; Hart, F. X. A Stable Thin-Film Lithium Electrolyte: Lithium Phosphorus Oxynitride. *J. Electrochem. Soc.* **1997**, *144*, 524–532.
- (21) Bates, J. B.; Dudney, N. J.; Gruzalski, G. R.; Zuhr, R. A.; Choudhury, A.; Luck, C. F.; Robertson, J. D. Fabrication and Characterization of Amorphous Lithium Electrolyte Thin Films and Rechargeable Thin-Film Batteries. *J. Power Sources* **1993**, *43*, 103–110.
- (22) Neudecker, B. J.; Dudney, N. J.; Bates, J. B. “Lithium-Free” Thin-Film Battery with in Situ Plated Li Anode. *J. Electrochem. Soc.* **2000**, *147*, 517–523.
- (23) Bates, J. B.; Dudney, N. J.; Neudecker, B.; Ueda, A.; Evans, C. D. Thin-Film Lithium and Lithium-Ion Batteries. *Solid State Ionics* **2000**, *135*, 33–45.
- (24) Li, J.; Ma, C.; Chi, M.; Liang, C.; Dudney, N. J. Solid Electrolyte: The Key for High-Voltage Lithium Batteries. *Adv. Energy Mater.* **2015**, *5*, No. 1401408.
- (25) Han, F.; Westover, A. S.; Yue, J.; Fan, X.; Wang, F.; Chi, M.; Leonard, D. N.; Dudney, N. J.; Wang, H.; Wang, C. High Electronic Conductivity as the Origin of Lithium Dendrite Formation within Solid Electrolytes. *Nat. Energy* **2019**, *4*, 187–196.
- (26) Le Van-Jodin, L.; Ducroquet, F.; Sabary, F.; Chevalier, I. Dielectric Properties, Conductivity and Li+ Ion Motion in LiPON Thin Films. *Solid State Ionics* **2013**, *253*, 151–156.
- (27) Su, Y.; Falgenhauer, J.; Polity, A.; Leichtweiß, T.; Kronenberger, A.; Obel, J.; Zhou, S.; Schlettwein, D.; Janek, J.; Meyer, B. K. LiPON Thin Films with High Nitrogen Content for Application in Lithium Batteries and Electrochromic Devices Prepared by RF Magnetron Sputtering. *Solid State Ionics* **2015**, *282*, 63–69.
- (28) Bates, J. B.; Dudney, N. J.; Gruzalski, G. R.; Zuhr, R. A.; Choudhury, A.; Luck, C. F.; Robertson, J. D. Electrical Properties of Amorphous Lithium Electrolyte Thin Films. *Solid State Ionics* **1992**, *53–56*, 647–654.
- (29) Nimisha, C. S.; Rao, K. Y.; Venkatesh, G.; Rao, G. M.; Munichandraiah, N. Sputter Deposited LiPON Thin Films from Powder Target as Electrolyte for Thin Film Battery Applications. *Thin Solid Films* **2011**, *519*, 3401–3406.
- (30) Wang, Y.; Liu, B.; Li, Q.; Cartmell, S.; Ferrara, S.; Deng, Z. D.; Xiao, J. Lithium and Lithium Ion Batteries for Applications in Microelectronic Devices: A Review. *J. Power Sources* **2015**, *286*, 330–345.
- (31) Fujibayashi, T.; Kubota, Y.; Iwabuchi, K.; Yoshii, N. Highly Conformal and High-Ionic Conductivity Thin-Film Electrolyte for 3D-

Structured Micro Batteries: Characterization of LiPON Film Deposited by MOCVD Method. *AIP Adv.* **2017**, 7, No. 085110.

(32) Lee, S. J.; Bae, J. H.; Lee, H. W.; Baik, H. K.; Lee, S. M. Electrical Conductivity in Li-Si-P-O-N Oxynitride Thin-Films. *J. Power Sources* **2003**, 123, 61–64.

(33) Lee, S. J.; Baik, H. K.; Lee, S. M. An All-Solid-State Thin Film Battery Using LISIPON Electrolyte and Si-V Negative Electrode Films. *Electrochem. Commun.* **2003**, 5, 32–35.

(34) Su, Y.; Falgenhauer, J.; Leichtweiß, T.; Geiß, M.; Lupó, C.; Polity, A.; Zhou, S.; Obel, J.; Schlettwein, D.; Janek, J.; et al. Electrochemical Properties and Optical Transmission of High Li⁺ Conducting LiSiPON Electrolyte Films. *Phys. Status Solidi B* **2017**, 254, No. 1600088.

(35) Hamon, Y.; Douard, A.; Sabary, F.; Marcel, C.; Vinatier, P.; Pecquenard, B.; Levasseur, A. Influence of Sputtering Conditions on Ionic Conductivity of LiPON Thin Films. *Solid State Ionics* **2006**, 177, 257–261.

(36) Zhao, S.; Fu, Z.; Qin, Q. A Solid-State Electrolyte Lithium Phosphorus Oxynitride Film Prepared by Pulsed Laser Deposition. *Thin Solid Films* **2002**, 415, 108–113.

(37) Vereda, F.; Goldner, R. B.; Haas, T. E.; Zerigian, P. Rapidly Grown IBA LiPON Films with High Li-Ion Conductivity and Electrochemical Stability. *Electrochem. Solid-State Lett.* **2002**, 5, A239–A241.

(38) Kim, Y. G.; Wadley, H. N. G. Lithium Phosphorous Oxynitride Films Synthesized by a Plasma-Assisted Directed Vapor Deposition Approach. *J. Vac. Sci. Technol., A* **2008**, 26, 174–183.

(39) Kim, H. T.; Mun, T.; Park, C.; Jin, S. W.; Park, H. Y. Characteristics of Lithium Phosphorous Oxynitride Thin Films Deposited by Metal-Organic Chemical Vapor Deposition Technique. *J. Power Sources* **2013**, 244, 641–645.

(40) Kozen, A. C.; Pearse, A. J.; Lin, C. F.; Noked, M.; Rubloff, G. W. Atomic Layer Deposition of the Solid Electrolyte LiPON. *Chem. Mater.* **2015**, 27, 5324–5331.

(41) Chantrell, P. G.; Popper, P. Inorganic Polymers and Ceramics. In *Special Ceramics*; Popper, P., Eds.; Academic Press, 1965; pp 87–102.

(42) Ayllett, B. J. Silicon–Nitrogen Polymers. *Special Ceramics*; In Popper, E. P., Eds.; Academic Press, 1964; p 105.

(43) Wynne, K. J.; Rice, R. W. Ceramics via Polymer Pyrolysis. *Annu. Rev. Mater. Sci.* **1984**, 14, 297–334.

(44) Brinker, C. J.; Clark, D. E.; Ulrich, D. R. In *Better Ceramics through Chemistry II*, Materials Research Society Symposium Proceedings, 1986.

(45) Brinker, C. J.; Clark, D. E.; Ulrich, D. R. In *Better Ceramics Through Chemistry III*, Materials Research Society Symposium Proceedings, 1988.

(46) Laine, R. M. *Transformation of Organometallics into Common and Exotic Materials: Design and Activation*; Springer, 1988.

(47) Laine, R. M.; Sellinger, A. Si-Containing Ceramic Precursors. *The Chemistry of Organic Silicon Compounds*; John Wiley & Sons, Ltd., 2003.

(48) Okamura, K. Ceramic Fibres from Polymer Precursors. *Composites* **1987**, 18, 107–120.

(49) Greil, P. Polymer Derived Engineering Ceramics. *Adv. Eng. Mater.* **2000**, 2, 339–348.

(50) Temeche, E.; Zhang, X.; Richard, M. L. Polymer Precursor Derived Li_xPON Electrolytes for Li–S Battery, Submitted for publication, 2020.

(51) Laine, R. M.; Babonneau, F. Preceramic Polymer Routes to Silicon Carbide. *Chem. Mater.* **1993**, 5, 260–279.

(52) Li, L.; Dunn, J. B.; Zhang, X. X.; Gaines, L.; Chen, R. J.; Wu, F.; Amine, K. Recovery of Metals from Spent Lithium-Ion Batteries with Organic Acids as Leaching Reagents and Environmental Assessment. *J. Power Sources* **2013**, 233, 180–189.

(53) Zhang, P.; Yokoyama, T.; Itabashi, O.; Suzuki, T. M.; Inoue, K. Hydrometallurgical Process for Recovery of Metal Values from Spent Lithium-Ion Secondary Batteries. *Hydrometallurgy* **1998**, 47, 259–271.

(54) Larson, R. W.; Day, D. E. Preparation and Characterization of Lithium Phosphorus Oxynitride Glass. *J. Non-Cryst. Solids* **1986**, 88, 97–113.

(55) Mascaraque, N.; Fierro, J. L. G.; Durán, A.; Muñoz, F. An Interpretation for the Increase of Ionic Conductivity by Nitrogen Incorporation in LiPON Oxynitride Glasses. *Solid State Ionics* **2013**, 233, 73–79.

(56) Fleutot, B.; Pecquenard, B.; Martinez, H.; Letellier, M.; Levasseur, A. Investigation of the Local Structure of LiPON Thin Films to Better Understand the Role of Nitrogen on Their Performance. *Solid State Ionics* **2011**, 186, 29–36.

(57) Pichonat, T.; Lethien, C.; Tiercelin, N.; Godey, S.; Pichonat, E.; Roussel, P.; Colmont, M.; Rolland, P. A. Further Studies on the Lithium Phosphorus Oxynitride Solid Electrolyte. *Mater. Chem. Phys.* **2010**, 123, 231–235.

(58) Stallworth, P. E.; Vereda, F.; Greenbaum, S. G.; Haas, T. E.; Zerigian, P.; Goldner, R. B. Solid-State NMR Studies of Lithium Phosphorus Oxynitride Films Prepared by Nitrogen Ion Beam-Assisted Deposition. *J. Electrochem. Soc.* **2005**, 152, A516–A522.

(59) Manzi, J.; Curcio, M.; Brutti, S. Structural and Morphological Tuning of LiCoPO₄ Materials Synthesized by Solvo-Thermal Methods for Li-Cell Applications. *Nanomaterials* **2015**, 5, 2212–2230.

(60) Ait Salah, A.; Jozwiak, P.; Zaghib, K.; Garbarczyk, J.; Gendron, F.; Mauger, A.; Julien, C. M. FTIR Features of Lithium-Iron Phosphates as Electrode Materials for Rechargeable Lithium Batteries. *Spectrochim. Acta, Part A* **2006**, 65, 1007–1013.

(61) See, K. A.; Leskes, M.; Griffin, J. M.; Britto, S.; Matthews, P. D.; Emly, A.; Van Der Ven, A.; Wright, D. S.; Morris, A. J.; Grey, C. P.; et al. Ab Initio Structure Search and in Situ 7Li NMR Studies of Discharge Products in the Li-S Battery System. *J. Am. Chem. Soc.* **2014**, 136, 16368–16377.

(62) Temeche, E.; Zhang, X.; Richard, M. L. Solid Electrolytes for Li-S Batteries. Solid Solutions of Polyethylene Oxide with Li_xPON and Li_xSiPON Based Polymers, submitted for publication, 2020.

(63) Muñoz, F.; Durán, A.; Pascual, L.; Montagne, L.; Revel, B.; Rodrigues, A. C. M. Increased Electrical Conductivity of LiPON Glasses Produced by Ammonolysis. *Solid State Ionics* **2008**, 179, 574–579.

(64) Alam, T. M.; Conzone, S.; Brow, R. K.; Boyle, T. J. 6Li, 7Li Nuclear Magnetic Resonance Investigation of Lithium Coordination in Binary Phosphate Glasses. *J. Non-Cryst. Solids* **1999**, 258, 140–154.

(65) Berger, S.; Bock, W.; Frenking, G.; Jonas, V.; Müller, F. NMR Data of Methyltitanium Trichloride and Related Organometallic Compounds. A Combined Experimental and Theoretical Study of MenXCl_{4-n} (n = 0–4; X = C, Si, Sn, Pb, Ti). *J. Am. Chem. Soc.* **1995**, 117, 3820–3829.

(66) Arshadi, M.; Johnels, D.; Edlund, U.; Ottosson, C. H.; Cremer, D. Solvated Silylium Cations: Structure Determination by NMR Spectroscopy and the NMR/Ab Initio/IGLO Method. *J. Am. Chem. Soc.* **1996**, 118, 5120–5131.

(67) Roh, N. S.; Lee, S. D.; Kwon, H. S. Effects of Deposition Condition on the Ionic Conductivity and Structure of Amorphous Lithium Phosphorus Oxynitrate Thin Film. *Scr. Mater.* **1999**, 42, 43–49.

(68) Albertus, P.; Babinec, S.; Litzelman, S.; Newman, A. Status and Challenges in Enabling the Lithium Metal Electrode for High-Energy and Low-Cost Rechargeable Batteries. *Nat. Energy* **2018**, 3, 16–21.